

Spatially uniform resistance switching of low current, high endurance titanium-niobium-oxide memristors

Suhas Kumar,¹ Noraica Davila,¹ Ziwen Wang,² Xiaopeng Huang,¹ John Paul Strachan,¹

David Vine,³ A. L. David Kilcoyne,³ Yoshio Nishi² and R. Stanley Williams¹

¹Hewlett Packard Labs, 1501 Page Mill Rd, Palo Alto, CA 94304, USA

²Stanford University, Stanford, CA 94305, USA

³Lawrence Berkeley National Laboratory, Berkeley, CA 94720, USA

Supplementary Material

Film growth

150 nm of Si₃N₄ was grown using low pressure chemical vapor deposition (LPCVD) on double side-polished Si wafer with low p-doping. Holes were etched into the Si wafer to allow free suspension of Si₃N₄ membranes. Detailed processing information is available elsewhere. [J. Appl. Phys. 118, 034502 (2015)] Crosspoint devices were lithographically patterned onto these membranes. The Pt electrodes were evaporated from a Pt target. The layers of Nb₂O₅+NbO₂+TiNO_{0.5} were sputter deposited using reactive sputtering. TiNO_x used throughout the manuscript (except as noted in Figure S4) was sputtered with a discharge power of 50 W, while that used in Figure S4 was sputtered using a lower discharge power of 25 W.

Spectral processing

Spectra were first normalized to background absorptions in the vacuum chamber, measured through a blank Si₃N₄ membrane (with no other material on it). The resulting spectra were corrected for a linear background in the pre-absorption-edge region. Peak fitting was done using the software Sigmaplot PeakFit (<http://www.sigmaplot.co.uk/products/peakfit/peakfit.php>). The pre-edge of the oxygen K-edge was

aligned to zero, a linear background in the pre-edge region was subtracted, and the data was smoothed by 1% using Savitsky-Golay smoothing. [Anal. Chem. 36, 1627 (1964)] The peaks were composed of a convolution of a Lorentzian component (to account for the broadening of spectral lines due to excited electron lifetime) and a Gaussian component (to account for the resolution of the spectrometer, mostly due to the beamline monochromator). For each spectrum, the component bands were allowed to vary in width, amplitude and position to obtain the best fit. Smoothing of data in Figures 3 and 4 was performed using Savitsky-Golay smoothing over 15 adjacent points.

Signal limits of the time-multiplexed system

The signal levels ($\sim 0.2\%$) shown in Figure 3 were near the limit of the technique due to multiple constraints. The most obvious way to improve signal was to dwell for longer at every pixel/energy. This increases the number of times the device must be able to switch states and also the time for which every spot on the sample is exposed to high-intensity x-rays. The former requirement needs higher endurance from the devices under investigation. In this study, our memristor devices exhibited endurences of at least several millions, which was sufficient for dwell times of >100 ms at every pixel of ~ 30 nm in diameter. The second constraint of extended exposure to x-rays resulted in carbon deposition on top of the exposed regions, a common problem with many focused probe techniques that operate in low vacuum; in this case the base pressure of the STXM chamber was about 10^{-5} torr. Over-exposure meant excessive carbon deposition and subsequent reduction in the x-ray signal. Owing mainly to these factors, the signal level on this particular STXM was limited to 0.1-0.2% over the background.

Uniformity of the signal within the crosspoint

We show that the signal within the crosspoint region is non-localized/uniform using multiple data analyses. First, the histograms of the data inside and outside the crosspoint region in different experiments (ON-OFF, Joule heating and electric field driven differences) appear to be single Gaussian functions (Figures 3 and S7) with the standard deviation/width of the distribution being similar both inside and outside the

crosspoint. This strongly suggests that the signal within the crosspoint was a shift in the zero-mean distribution outside the crosspoint, without any spatial features. The Joule heating studied at different voltages over different regions within the crosspoint (Figure S10) show similar signals in the different regions. This is another indication of the uniformity of the signal. The autocorrelation, Poincare plots and the Fourier transforms of the signal within the crosspoint further supported this conclusion (Figures S11-S13).

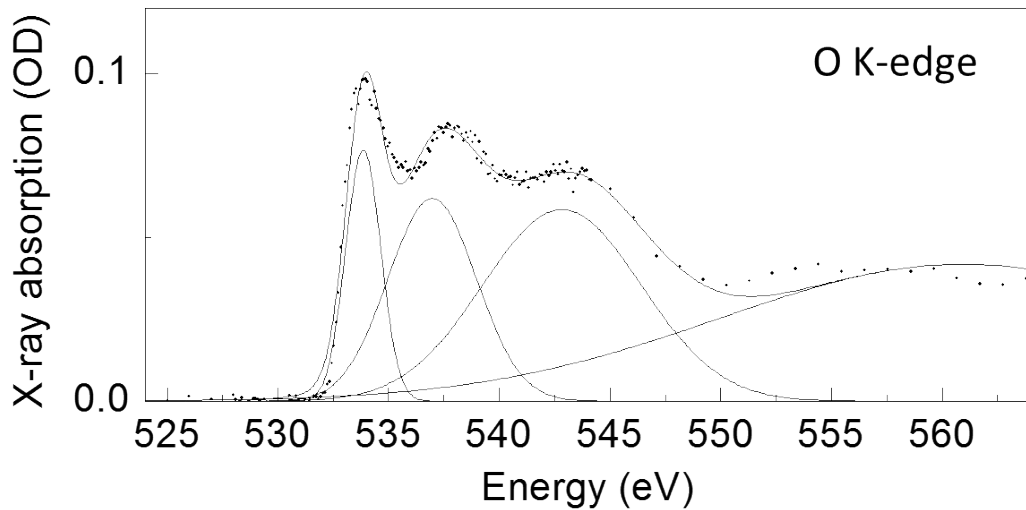


Figure S1: As-grown NbO₂. O K-edge spectrum of as-grown NbO₂ (not in interface with any other oxides). The prominent bands of NbO₂ are clearly visible and identifiable. [Solid State Comm. 87, 699 (1993)] this can be compared with the spectrum of the device stack (with niobium and titanium oxides) to identify the bands originating from Nb-O bonds.

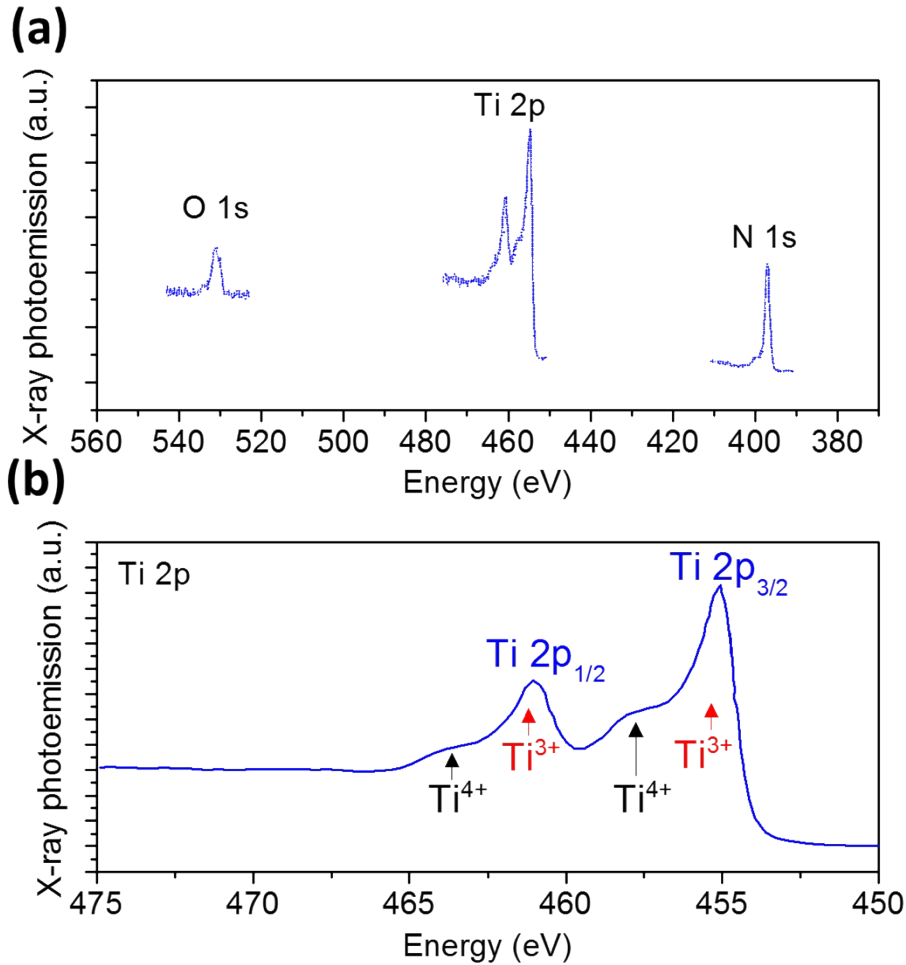


Figure S2: As-grown titanium oxynitride. (a) X-ray photoemission spectra of the O 1s, Ti 2p and N 1s peaks (as indicated) from an as-deposited film of titanium oxynitride layer with no other oxide present. The stoichiometry of the film was determined to be $\text{TiN}_{1.0}\text{O}_{0.5}$ (with an error on the composition fractions of <10%). (b) Magnified plot of the Ti L-edge spectrum from (a) showing that a majority of the Ti atoms were in the 3+ oxidation state, with a minority of them in the 4+ oxidation state. It is plausible that the power-driven sputtering of this film onto the underlying niobium oxide layers during fabrication of a cell stack drove some of the Ti ions into the niobium oxide layers, thereby intermixing the two layers and causing further oxidation of Ti.

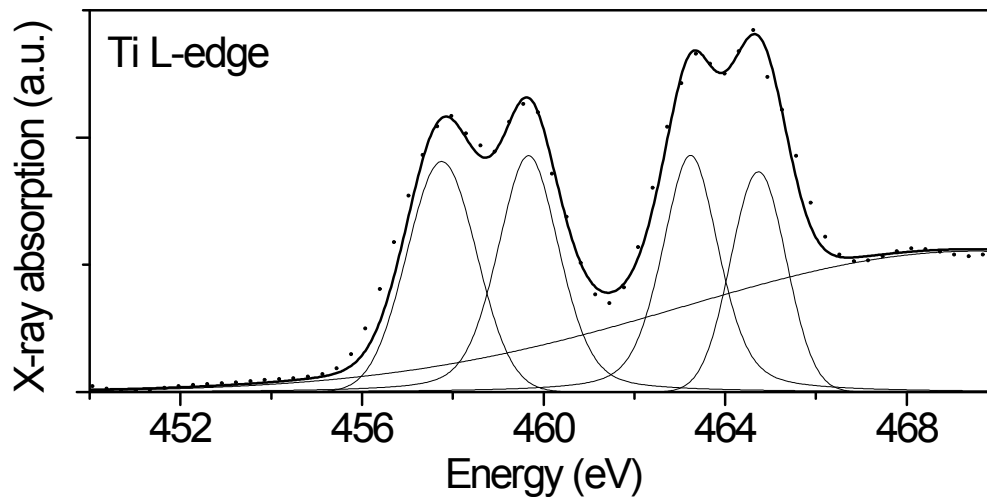


Figure S3: Ti spectrum through the cell stack. Ti L-edge absorption spectrum (obtained using x-ray transmission) through the cell stack of the un-operated cell shown in Figure 1a. This spectrum shows that the oxidation state of the Ti was mixed between 4+ and 3+, consistent with photoemission data in Figure S2.

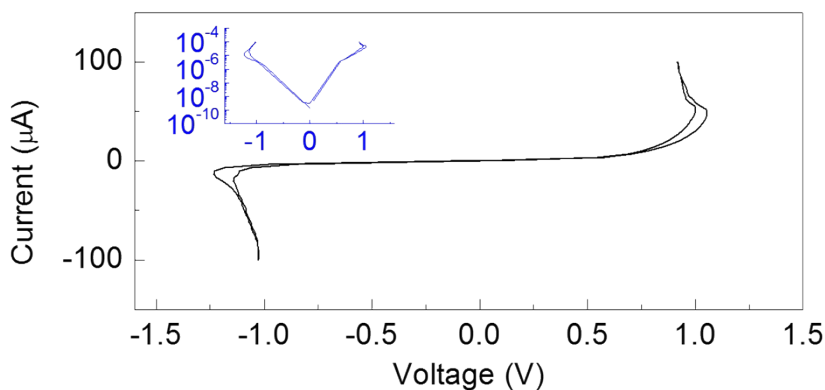


Figure S4: Current-voltage plot of identical devices with low-power TiNO_x . Current voltage characteristics (using current sweep) of a cell that consisted of identical material stack and geometry, with the TiNO_x layer having been deposited with lower power/energy. This was done intentionally to prevent the Ti from penetrating the underlying niobium oxide layer and thereby also preventing the further oxidation of Ti (possibly preventing formation of TiO_x). This device exhibits negative differential

resistance, which is a desirable non-linear property in selector applications. Inset is the same plot in a semi-logarithmic scale. The low currents at lower voltages (<0.5 V) owing to the non-linearity in conductance allowed for current limiting capability of the memristors studied in this paper. In this work, static current-voltage plots are measured by sweeping current to prevent a run-away current overshoots during a voltage sweep, which was found to damage the devices. Applying voltage pulses for shorter durations did not degrade or damage the devices as much.

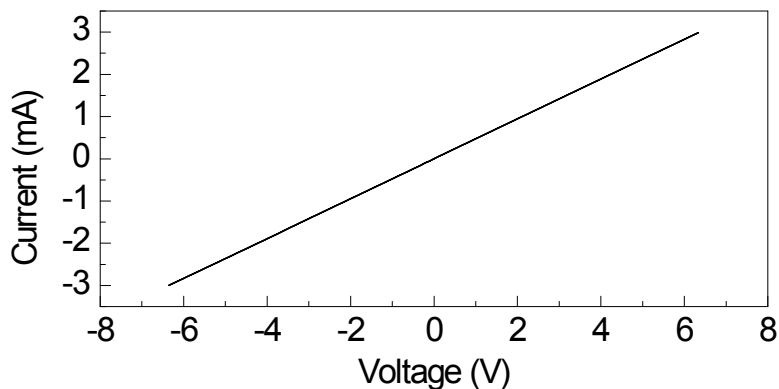


Figure S5: Current-voltage plot of TiNO_x only. Current voltage characteristics (using current sweep) of a cell that consisted of only the TiNO_{0.5} layer between Pt electrodes. The highly linear behavior showing no resistance switching is indicative of the highly conductive nature of the TiNO_{0.5} layer relative to the NbO_x layers. Since TiNO_x alone does not exhibit resistive switching or non-linear behavior, we argue that the interface between TiNO_x and NbO_x was important in causing resistive switching.

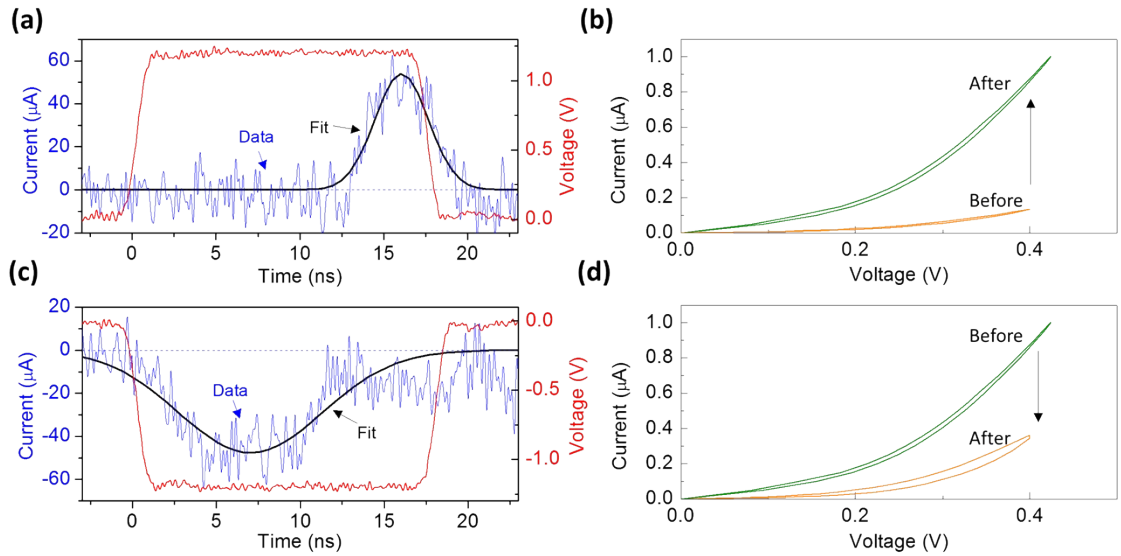


Figure S6: High speed switching. (a) SET operation by application of a positive voltage pulse on a fresh cell (different from the one used in the STXM studies). Black curve is a fit to the current transient used to calculate the area under the curve. The area multiplied by the applied voltage was found to be ~ 300 fJ (75 fJ/ μm^2). (b) Static current-voltage behavior of the cell before and after the SET operation, confirming non-volatile resistance change. (c)-(d) RESET operation of the same cell by application of a negative voltage pulse. The area under the current transient multiplied by the applied voltage was found to be ~ 700 fJ (175 fJ/ μm^2). (c) Static current-voltage behavior of the cell before and after the RESET operation, confirming non-volatile resistance change. A portion of the measured switching energy was used to charge the parasitic capacitance in the cell and wires, which was non-negligible given the micrometer scale of the devices. Hence, upon scaling down to nanometer scales, we expect the switching energy to scale essentially with cell area.

From the cell geometry and approximations of the dielectric constants, we estimate that the capacitance of the structure to be >5 fF. This capacitor will consume an energy of >2 fJ to charge during the operation described in Figure S6. Hence, most of the energy reported in Figure S6 was likely used to perform the resistance switching. We note that the maximum power in the data displayed in Figure S6 is about 60 μW , while that recorded for static switching (Figure 1) was <3 μW . This significant different could originate

from the devices being made to switch in the sub-25 ns timescale, and possibly also the high-power transients that were not recorded in the static data displayed in Figure 1.

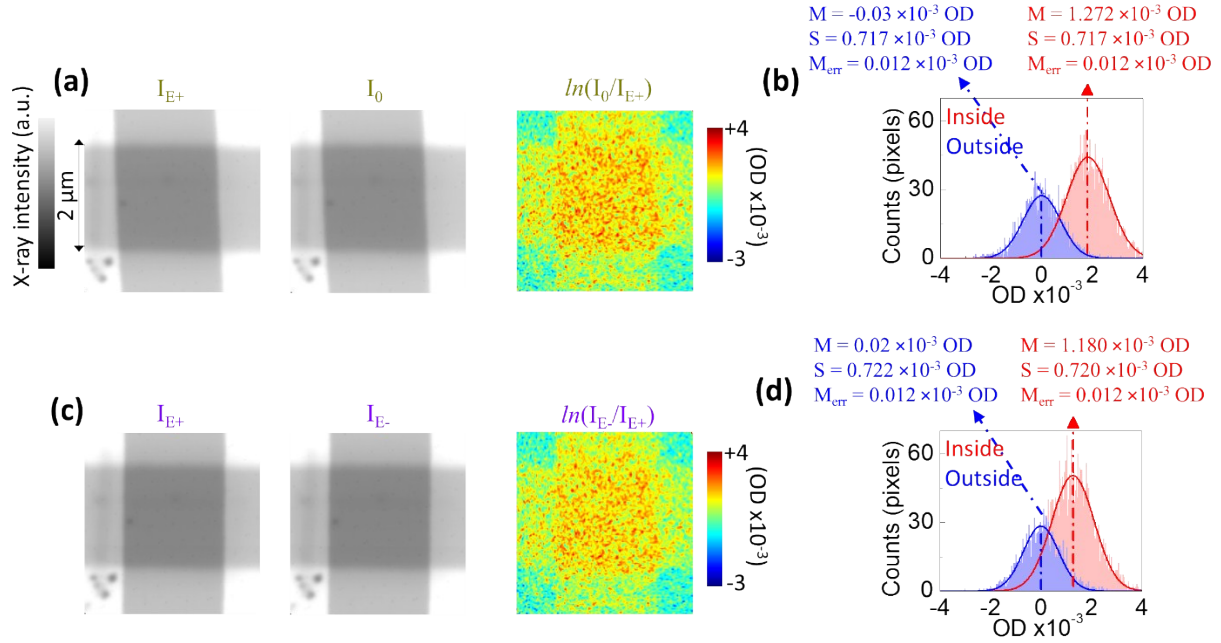


Figure S7: Raw data of Figures 4a-4d and corresponding histograms. (a) Raw intensity maps of the cell corresponding to Figure 4a. Ratio shown in Figure 4a is reproduced. (b) Histogram of the data inside and outside the crosspoint region of the ratio map in (a). Solid lines are Gaussian fits. Dashed vertical lines indicate the mean of the distribution. The mean along with the error inside the crosspoint is noted. (c) Raw intensity maps of the cell corresponding to Figure 4c. Ratio shown in Figure 4c is reproduced. (d) Histogram of the data inside and outside the crosspoint region of the ratio map in (c). Solid lines are Gaussian fits. Dashed vertical lines indicate the mean of the distribution. The mean (M), standard deviation (S) and the standard error of the mean ($M_{err}=S/\sqrt{N}$) are noted for both histograms in (b) and (d). N is the number of pixels within the crosspoint over which the data was acquired. Histograms in Figures 3 and S7 were obtained using 20,000 bins over the data range. The dark spots seen towards the bottom left corner (outside the crosspoint) in the raw maps are carbon deposits from the previous x-ray mapping on this cell, which did not affect cell behavior.

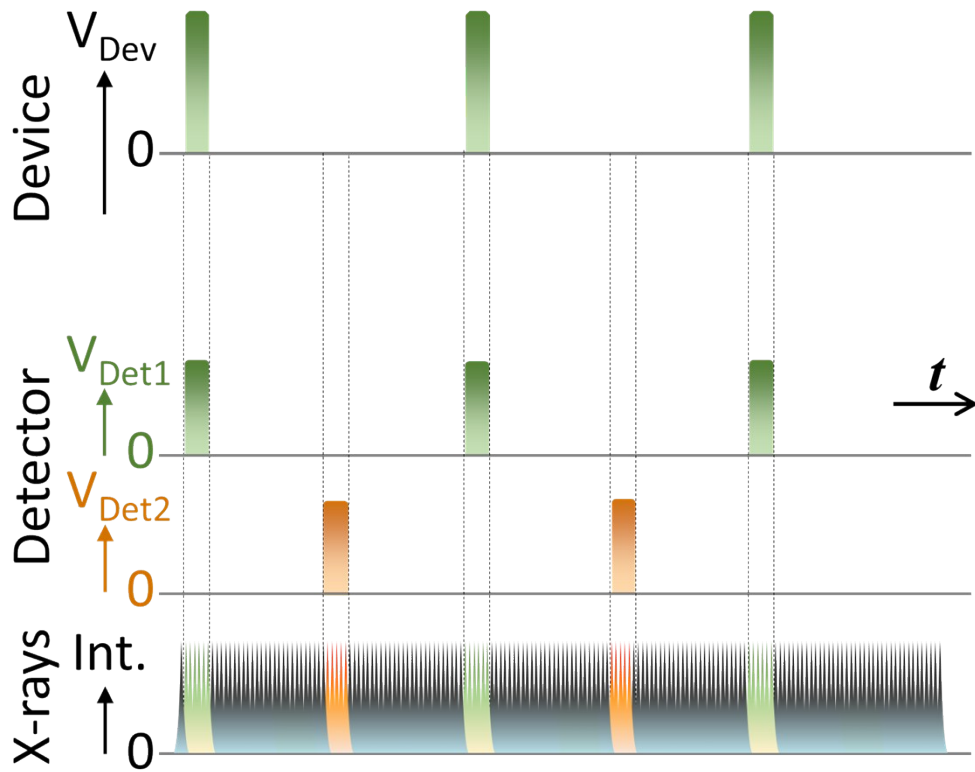


Figure S8: Joule heating effect. Time-multiplexed scheme applied to the cell to measure its response to Joule heating. This is a modification of the scheme shown in Figure 2b. The two sets of measurements are done (1) during application of a positive voltage pulse and (2) during application of no voltage pulse. See [J. Appl. Phys. 118, 034502 (2015)] for further details.

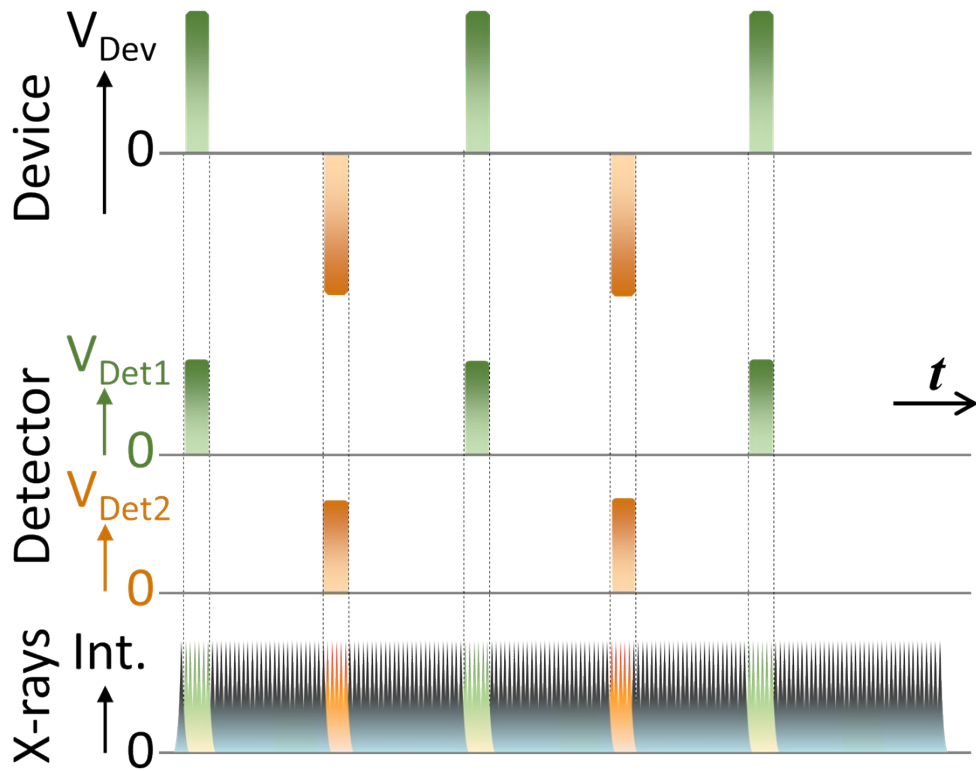


Figure S9: Electric-field effect. Time-multiplexed scheme applied to the cell to measure its response to electric field. This is a modification of the scheme shown in Figure 2b. The two sets of measurements are done (1) during application of a positive voltage pulse and (2) during application of a negative voltage pulse. See [J. Appl. Phys. 118, 034502 (2015)] for further details.

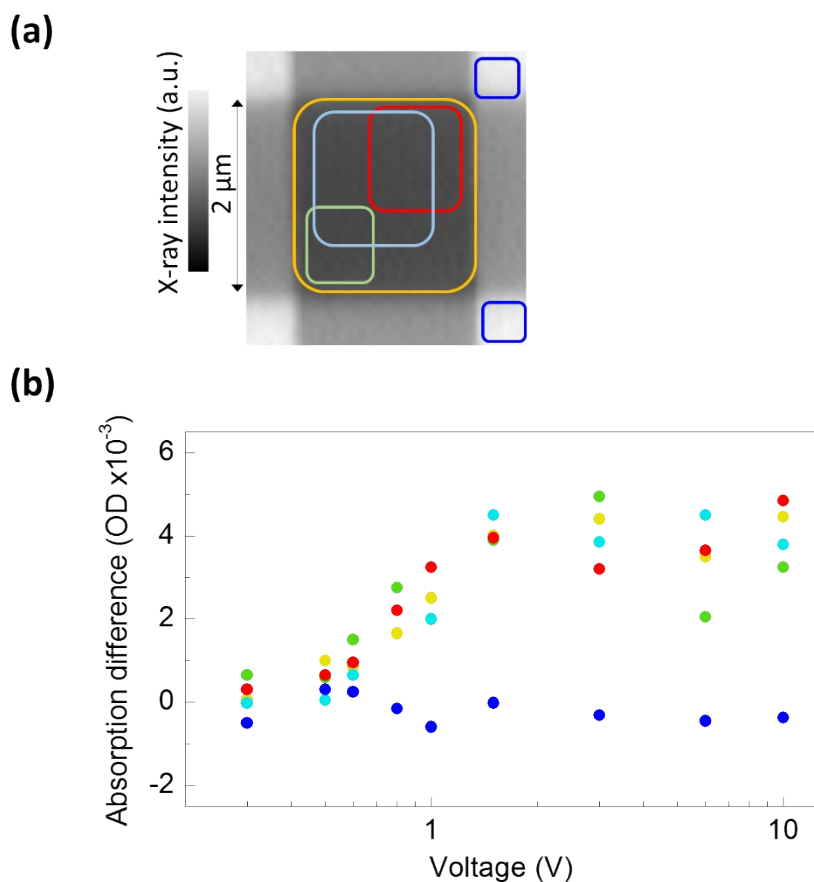


Figure S10: Joule heating at different voltages. (a) X-ray intensity map of a fresh device, different from the one studied throughout the rest of this work. Approximate regions within which Joule heating effects were studied are marked. (b) The averaged signal within the different regions marked in (a) at different voltage amplitudes (in logarithmic scale) of the applied pulses (compared to no applied voltage pulse). The different regions exhibit an increasing signal with applied voltage and thus power. This consistency is a reaffirmation of the spatially uniform nature of the changes. There is saturation of the signal at about 1.5 V. This may be due to the limited temperature range for which the material exhibits spectral changes, or the current being controlled by the parasitic/electrode resistances at higher voltages. The signal outside the crosspoint is essentially unaffected by the applied voltages

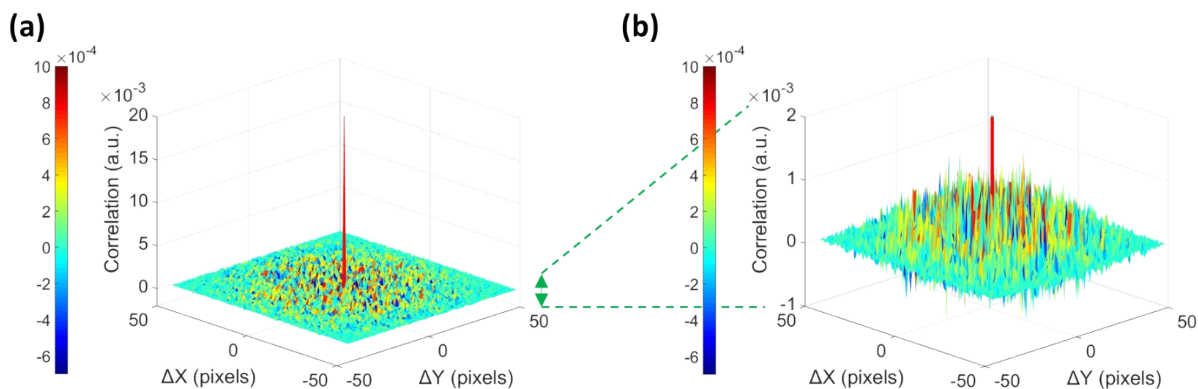


Figure S11: Autocorrelation of the signal within the crosspoint. (a) The 2D autocorrelation function of the matrix of pixels within the crosspoint region of the data in Figure 4a. The plot is essentially that expected from a random function, wherein the only high correlation is at the origin (or zero shift), whereas the rest of the region shows very weak spatial correlation. (b) Expanded view to make this observation clear.

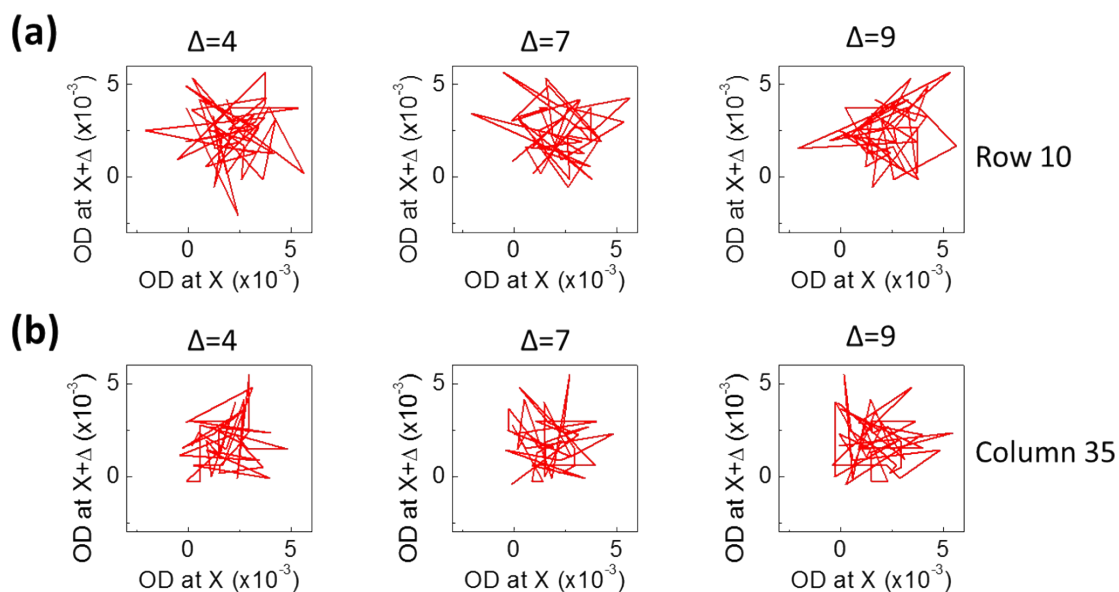


Figure S12: Poincare plots of the signal within the crosspoint Poincare plots along (a) a randomly chosen row and (b) a randomly chosen column are displayed using different pixel increments (Δ). Poincare plots of the data within the different rows and columns of the pixel matrix within the crossbar region showed no recognizable features, indicating randomness, or noise, within the crossbar, along with a constant offset/signal.

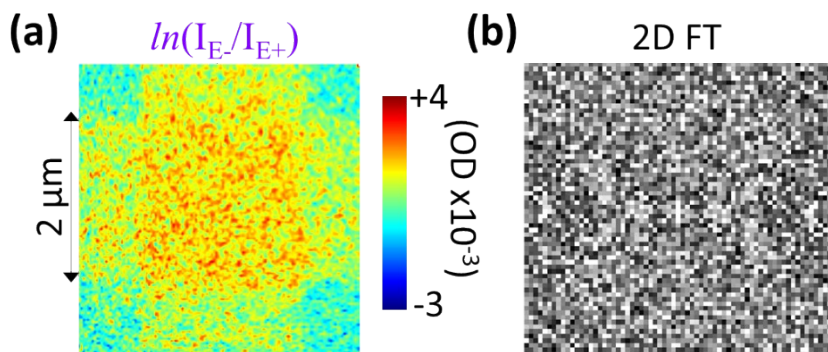


Figure S13: Fourier transform of the signal within the crosspoint. (a) Reproduction of the data in Figure 4a. (b) 2D Fourier transform of the data within the crosspoint region showing no recognizable features, indicating a uniformly distributed signal.

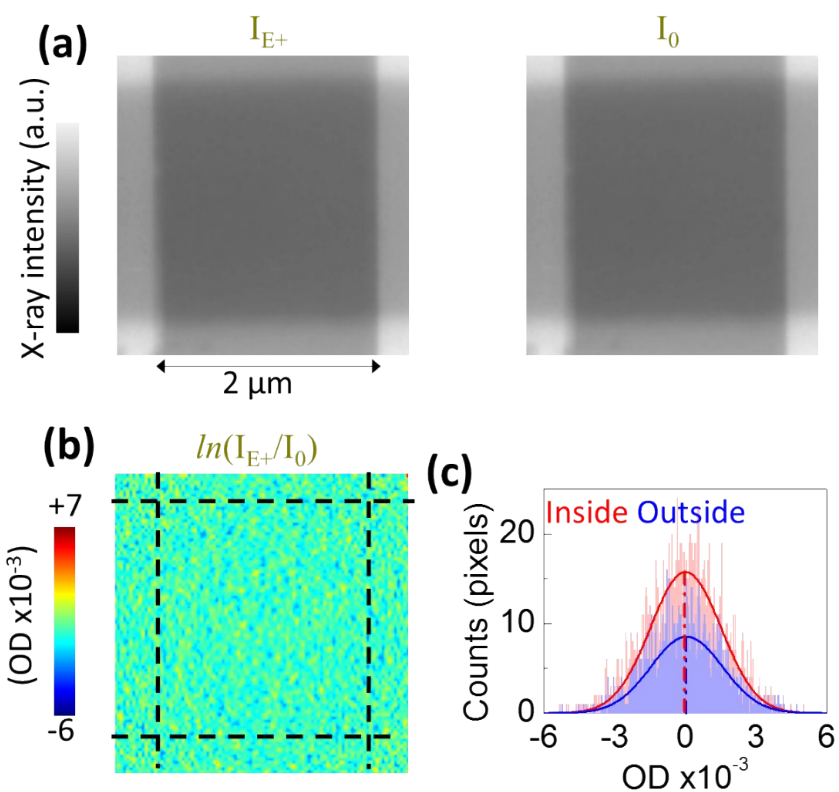


Figure S14: Signal upon Joule heating with very low voltage. (a)-(b) X-ray intensity maps of the cell (I_{E^+} and I_0) along with their logarithmic ratio (in the units of optical density, or OD) with applied voltage $E_+=0.2$ V. Dashed lines are approximate boundaries of the electrodes. (c) Histogram of the data inside and

outside the crosspoint region. Solid lines are Gaussian fits. Dashed vertical lines indicate the mean of the distribution.

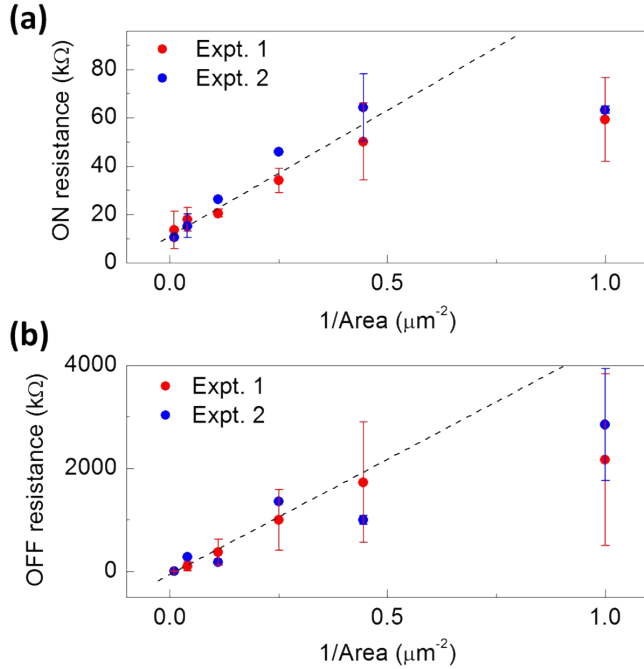


Figure S15: Area-scaling. (a) ON resistance of multiple devices obtained over multiple switching cycles (controlled using voltage pulses) across different lateral crosspoint areas. (b) OFF resistance of multiple devices obtained over multiple switching cycles (controlled using voltage pulses) across different lateral crosspoint areas. Dashed lines are linear fits to the data, except the data at the abscissa value of 1.0, which we considered an outlier (likely because of the lithographic imperfections in fabricating devices of such a small size).

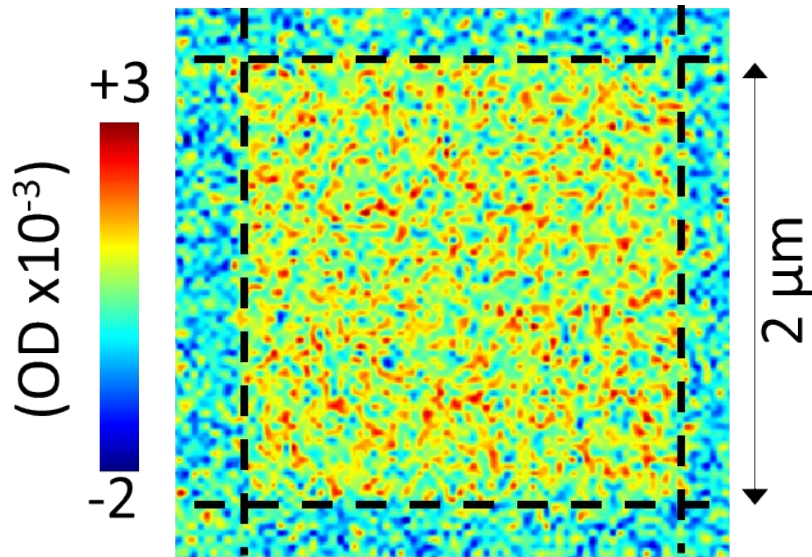


Figure S16: X-ray map of Figure 3c after additional processing. It can be noticed in Figure 3c (logarithmic ratio of ON and OFF x-ray maps) that there is some smaller signal from the electrodes as well, apart from that within the crosspoint area. Resistive switching is expected to occur only within the crosspoint area, while the signal from the electrodes are likely to not have directly contributed to the resistance switching. Hence, we subtracted the signal from the electrodes (using the mean of the signal within each electrode) within both electrodes (including the crosspoint area), resulting in the map presented here. This map confirms that there was a significant signal within the crosspoint after the smaller signal from the electrodes had been subtracted.